Optimal Arrangement Design of a Tube Bundle in Cross-Flow Using Computational Fluid Dynamics and Multi-Objective Genetic Algorithm

Ya Ge
School of Energy and Power Engineering,
Huazhong University of Science and Technology,
Wuhan 430074, China

Feng Xin
School of Energy and Power Engineering,
Huazhong University of Science and Technology,
Wuhan 430074, China

Yao Pan
The China Academy of Launch Vehicle Technology,
Beijing 100076, China

Zhichun Liu[1]
School of Energy and Power Engineering,
Huazhong University of Science and Technology,
Wuhan 430074, China
e-mail: zcliu@hust.edu.cn

Wei Liu
School of Energy and Power Engineering,
Huazhong University of Science and Technology,
Wuhan 430074, China

Recently, energy saving problem attracts increasing attention from researchers. This study aims to determine the optimal arrangement of a tube bundle to achieve the best overall performance. The multi-objective genetic algorithm (MOGA) is employed to determine the best configuration, where two objective functions, the average heat flux q and the pressure drop Δp, are selected to evaluate the performance and the consumption, respectively. Subsequently, a decision maker method, technique for order preference by similarity to an ideal solution (TOPSIS), is applied to determine the best compromise solution from noninferior solutions (Pareto solutions). In the optimization procedure, all the two-dimensional (2D) symmetric models are solved by the computational fluid dynamics (CFD) method. Results show that performances alter significantly as geometries of the tube bundle changes along the Pareto front. For the case 1 (using staggered arrangement as initial), the optimal q varies from 2708.27 W/m^2 to 3641.25 W/m^2 and the optimal Δp varies from 380.32 Pa to 1117.74 Pa, respectively. For the case 2 (using in-line arrangement as initial), the optimal q varies from 2047.56 W/m^2 to 3217.22 W/m^2 and the optimal Δp varies from 181.13 Pa to 674.21 Pa, respectively. Meanwhile, the comparison between the optimal solution with maximum q and the one selected by TOPSIS indicates that TOPSIS could reduce the pressure drop of the tube bundle without sacrificing too much heat transfer performance. [DOI: 10.1115/1.4043570]

Keywords: heat transfer enhancement, multi-objective optimization, configuration design, tube bundle, best compromise solution

1 Introduction

In order to meet the environmental and economic requirements, it is urgent to improve the heat transfer performance and reduce the fluid power consumption in the transport processes. Since the tube bundle is a vital part of the cross-flow heat exchangers, considerable optimization work including both the tube side and shell side have been done in recent decades [1–5]. Žukauskas [1] reported extensive experimental data for viscous flow across in-line and staggered tube bundles and developed a series of correlations for the wide range of Reynolds numbers. Matos et al. [2] optimized the geometry of staggered tubes in forced convection by the numerical method, and their study showed that there will always be an optimal spacing between rows of tubes for both the circular and elliptic tubes heat exchangers. Khan et al. [3] analytically studied the tube bundle and found that compact bundles could give higher heat transfer rates than widely spaced ones. Thus, to improve the performances of the tube bundle, a practical method is to arrange tubes appropriately.

However, the studies mentioned above and other investigations including the shell-and-tube heat exchanger [6,7], the heat sink [8,9], or the tube insert [10–12] show a common phenomenon that the flow resistance often increases with the enhancement of heat transfer. Therefore, resolving these two conflicting objectives is crucial in the optimization process. Researchers put forward some evaluation criteria to evaluate the overall performance of the heat exchanger, such as performance evaluation criteria [13], JF factor [14], and efficiency evaluation criterion [15]. These evaluation criteria sometimes conflict with each other, which means it is difficult to establish a generally applicable selection criterion. Recently, multi-objective optimization techniques draw extensive attention in optimization studies. For different situations, it is possible to apply multi-objective optimization techniques, such as multi-objective genetic algorithm (MOGA) [16], to obtain noninferior solutions, and then choose the most feasible solution to meet the requirements. This approach has been proven to be effective, and gradually applied in the optimization design of different fields [17–20].

In the optimization procedure, an efficient method to speed up the entire process is to use surrogate models, such as response surface methods [21,22], artificial neural network [23,24], support vector machine [25,26], instead of computational fluid dynamics (CFD) models. However, surrogate methods are computationally efficient, but might not find the real optimal solution due to the limit of prediction from these models. Nowadays, with the improvement of computer performance, coupling the CFD software and optimization algorithm attracts increasing attention from researchers. For instance, Cheng et al. [27] used the simplified conjugate-gradient method [28] and the finite element method to design the shape of air channels. Liu et al. [29] also solved a geometric optimization problem for a two-stage thermoelectric module by this method. Daróczy et al. [30] coupled ANSYS-FLUENT and the MOGA to optimize the arrangement of seven tubes for a laminar, two-dimensional (2D) problem. Ge et al. [31,32] applied both the CFD software COMSOL MULTIPHYSICS and the MOGA to optimize the geometry and the shape profile for a laminar-flow heat sink to achieve the high overall performance.

[1]Corresponding author.

Contributed by the Heat Transfer Division of ASME for publication in the JOURNAL OF HEAT TRANSFER. Manuscript received November 23, 2018; final manuscript received April 11, 2019; published online May 14, 2019. Assoc. Editor: Danesh K. Tafti.

Undoubtedly, the application of the optimization algorithm and CFD software can improve the performance of the tube bundle with more accuracy. Nevertheless, to the best of our knowledge, there is no arrangement optimization study for the tube bundle in turbulent flow in the existing literature, where the CFD software, the MOGA, and the decision maker technique are applied to find the best compromise solution. The motivation of this study is based on the following two aspects: on the one hand, the arrangement of tube bundles in turbulent flow plays an indispensable role in energy saving, while combining the multi-objective algorithm and the decision maker approach is possible to design a high-performance tube bundle in a more general way; on the other hand, the accuracy of the direct problem is critical for the optimal solution, which means using CFD models is more practical than surrogate models. Based on the above background, this study applies an optimization approach coupling the finite element method and the MOGA to achieve the arrangement of tube bundles with best performances. Two conflicting objective functions, the pressure drop between the inlet and outlet Δp and the average heat flux of tubes q, are selected to be optimized simultaneously. Meanwhile, the 2D symmetric model is established and solved by the COMSOL MULTIPHYSICS where the k–ε model is adopted to simulate the turbulent flow. In the multi-objective optimization procedure, noninferior solutions (Pareto front) with optimal coordinate values are obtained in the MATLAB environment. Subsequently, a decision making technique, technique for order preference by similarity to an ideal solution (TOPSIS) [33] is employed to determine the best compromise solution from the Pareto front.

2 Models and Governing Equations

2.1 Problem Description. The problem under consideration is the forced convection heat transfer for a tube bundle. The tubes might be arranged in the staggered or in-line model, as the corresponding computational domain is shown in Fig. 1(*a*) or Fig. 1(*b*), respectively. In tube bundles, the outer diameter D is taken as the characteristic length, while the flow characteristics are determined by the mean velocity in the minimum free cross section $\overline{u}$ rather than the inlet velocity u_{in}. Hence, the Reynolds number is defined on the basis of mean velocity as

$$\text{Re} = \frac{\rho \overline{u} \text{D}}{\mu} \tag{1}$$

In this study, air enters the domain at $T_{\text{in}} = 288.15\,\text{K}$ with inlet velocity $u_{\text{in}} = 6\,\text{m/s}$ ($\overline{u}$ is 12 m/s and $\text{Re} = 13{,}000$, correspondingly), while the outlet boundary is set to be pressure outlet $p_{\text{out}} = 0\,\text{Pa}$ since different inlet and outlet boundary conditions could improve the convergence of numerical models in COMSOL MULTIPHYSICS. All the tubes are supposed to have a constant outer wall temperature $T_{\text{w}} = 313.15\,\text{K}$ and air flow is warmed up by these tubes. The top and bottom boundaries are set to be symmetric boundary condition in order to save the computation time.

Besides, according to Ref. [1], the average heat transfer coefficient for the entire tube bank depends on the number of tube rows along the flow N. When $N \geq 16$, the flow will be fully developed and average heat transfer coefficient also will be constant. Hence, the computational domain consists 16 rows of tubes and then extended to 650 mm to suppress backflow.

In this study, the first two rows of tubes are selected as the design unit to be optimized and they can be placed arbitrarily in a limited area. Subsequently, all the other tubes are placed according to the arrangement configuration of the unit. Considering the symmetry of the structure, we set four coordinates as design variables. Geometric parameters and center coordinates are presented in Tables 1 and 2, respectively.

2.2 Governing Equations. The fluid is regarded as the nonisothermal, steady-state, incompressible turbulent flow, which means the governing equations are:

Continuity

$$\frac{\partial u}{\partial x} + \frac{\partial v}{\partial y} = 0 \tag{2}$$

Momentum in x-direction

$$\rho\left(u\frac{\partial u}{\partial x} + v\frac{\partial u}{\partial y}\right) = -\frac{\partial p}{\partial x} + \nabla \cdot (\mu \nabla u) \tag{3}$$

Momentum in y-direction

$$\rho\left(u\frac{\partial v}{\partial x} + v\frac{\partial v}{\partial y}\right) = -\frac{\partial p}{\partial y} + \nabla \cdot (\mu \nabla v) \tag{4}$$

Energy

$$\rho c_p\left(u\frac{\partial T}{\partial x} + v\frac{\partial T}{\partial y}\right) = \nabla \cdot (\lambda \nabla T) \tag{5}$$

where the gradient operator is represented by $\nabla = \mathbf{i}(\partial/\partial x) + \mathbf{j}(\partial/\partial y)$.

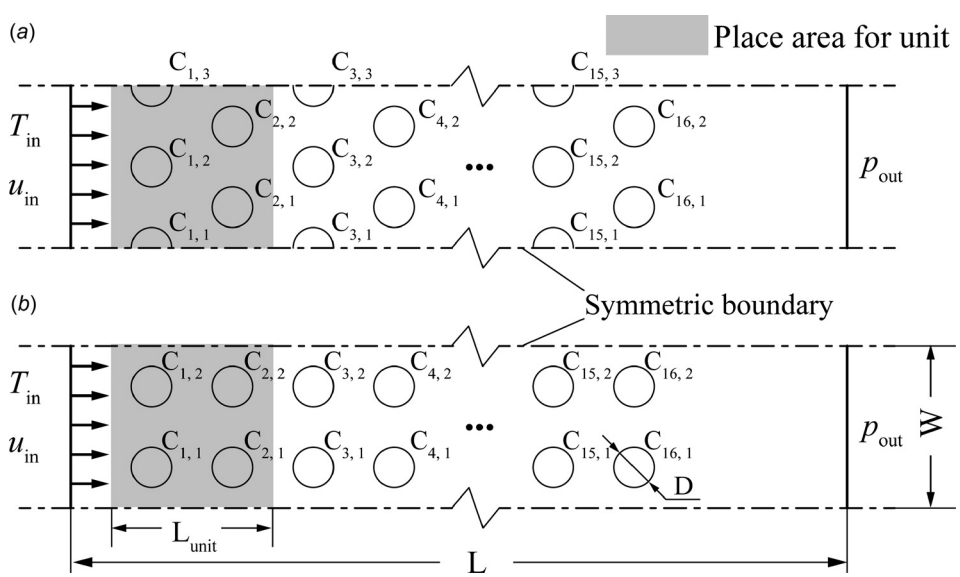

Fig. 1 Schematic of the forced convective heat transfer cases. (*a*) Cases 1, staggered arrangement as initial case and (*b*) cases 2, in-line arrangement as initial case.

Table 1 Structural parameters of the tube bundle in the channel

Geometric parameter	Value
Tube diameter, D	16.4 mm
Initial transverse pitch	$2 \times D$
Initial longitudinal pitch	$2 \times D$
Place area length	$4 \times D$
Channel width	$4 \times D$
Channel length	650 mm

Considering the flow is fully turbulent (Reynolds number $\mathrm{Re} > 10{,}000$), the standard k–ε model is adopted in this work to balance the computational resource and accuracy, which is presented as [34]:

Turbulent kinetic energy part

$$\rho \frac{\partial(ku_i)}{x_i} = \frac{\partial}{\partial x_j}\left[\left(\mu + \frac{\mu_t}{\sigma_k}\right)\frac{\partial k}{\partial x_j}\right] + G_k - \rho\varepsilon \tag{6}$$

Turbulent energy dissipation part

$$\rho \frac{\partial(\varepsilon u_i)}{x_i} = \frac{\partial}{\partial x_j}\left[\left(\mu + \frac{\mu_t}{\varepsilon}\right)\frac{\partial \varepsilon}{\partial x_j}\right] + \frac{C_{1\varepsilon}\varepsilon}{k}G_k - C_{2\varepsilon}\rho\frac{\varepsilon^2}{k} \tag{7}$$

where k is turbulent kinetic energy, ε is turbulent dissipation rate, G_k is producing term of turbulent kinetic energy generated by mean velocity gradient, μ_t is calculated by

$$\mu_t = \rho C_\mu \frac{k^2}{\varepsilon} \tag{8}$$

The model constants $C_{1\varepsilon}$, $C_{2\varepsilon}$, C_μ, σ_k, and σ_ε in the above equations use the default values: $C_\mu = 0.09$, $C_{1\varepsilon} = 1.44$, $C_{2\varepsilon} = 1.92$, $\sigma_k = 1.0$, $\sigma_\varepsilon = 1.3$.

The above governing equations along with the boundary conditions are solved by adopting the finite element method, where corresponding thermophysical properties are presented in Table 3. In this study, the direct problem is solved by commercial software, COMSOL MULTIPHYSICS. For a single simulation, the flow and temperature field are computed with approximately 90,000 degrees-of-freedom (DOF). All the simulations are done on a workstation (Sugon, Tianjin, China) with two 6-core CPUs (E5-2620 v2) (Intel, Santa Clara, CA) and 64 GB RAM (Samsung, Seoul, South Korea). Under such conditions, it takes approximately 2 min to complete a single simulation and 400 h to complete the entire multi-objective optimization procedure for staggered and in-line cases.

3 Optimization

3.1 Multi-Objective Genetic Algorithm. The genetic algorithm is one of the evolutionary algorithms, which mimic the principle of neo-Darwinian evolution. Based on this principle, individuals (i.e., solutions) compete with each other and the next-generation population will be generated according to the fitness values (i.e., objective function values) of their parent generation, which will gradually lead to a better offspring. Consequently, solutions continue to be optimized until a solution is found that satisfies minimum criteria.

When multiple conflicting objective functions exist in the optimization work, it is impossible to obtain a solution with all objective functions at their optimal values. In this case, one can obtain solutions that cannot be improved in any of the objectives without worsening at least one of the other objectives. These solutions are called noninferior solutions or Pareto solutions. The set of all Pareto solutions is referred to the Pareto front.

In this study, the goal is to find the optimal configuration of a tube bundle that maximizes heat transfer and minimizes pressure drop simultaneously. Therefore, two objective functions in the multi-objective optimization are described as follows:

$$J_1 = -q, \quad J_2 = \Delta p = p_{\text{in}} - p_{\text{out}} \tag{9}$$

where q is the average heat flux of all tubes, p_{in} and p_{out} are the inlet and outlet pressure, respectively. Subsequently, an efficient multi-objective evolutionary algorithm, the nondominated sorting genetic algorithm (NSGA-II) [16], is employed to optimize two objective functions defined above, where the main parameters used by MOGA are listed in Table 4. Therefore, a tube bundle with low pressure drop and high heat transfer performance can be achieved as J_1 and J_2 are approaching minimum values. Besides, according to Table 4, it could be inferred that the CFD codes need to be executed 6000 times for each optimization case.

3.2 Optimization Procedure. The procedure for optimizing the arrangement of tube bundles is illustrated in the flowchart shown in Fig. 2. When the geometry keeps changing in the optimization procedure, some infeasible situations, such as too close or even intersected circles (center distance $\overline{CiCj} < 21.4$ mm), and divergent solutions, may occur in the optimization procedure. In order to solve this problem, we introduced a penalty function in the optimization procedure, which means that all the infeasible solutions are intentionally given poor fitness values. Therefore, ill-conditioned individuals will be gradually eliminated as the process continues.

Table 2 Center coordinates of discrete tubes for staggered and in-line tube bundles

Model	Tube number ($i = 1, 2, \ldots, 8$)	Center coordinate (mm) (x, y)
Staggered	$C_{2i-1,\,1}$	$(a_1 + 65.6 \times (i-1), 0)$
	$C_{2i-1,\,2}$	$(a_2 + 65.6 \times (i-1), 32.8)$
	$C_{2i-1,\,3}$	$(a_1 + 65.6 \times (i-1), 65.6)$
	$C_{2i,\,1}$	$(a_3 + 65.6 \times (i-1), a_4)$
	$C_{2i,\,2}$	$(a_3 + 65.6 \times (i-1), 65.6 - a_4)$
In-line	$C_{2i-1,\,1}$	$(a_1 + 65.6 \times (i-1), a_2)$
	$C_{2i-1,\,2}$	$(a_1 + 65.6 \times (i-1), 65.6 - a_2)$
	$C_{2i,\,1}$	$(a_3 + 65.6 \times (i-1), a_4)$
	$C_{2i,\,2}$	$(a_3 + 65.6 \times (i-1), 65.6 - a_4)$

Table 3 Thermophysical properties of the air flow

Parameter	c_p (J kg^{-1} K^{-1})	μ (N·s m^{-2})	ρ (kg m^{-3})	λ (W m^{-1} K^{-1})
Value	1005	1.810×10^{-5}	1.205	2.59×10^{-2}

4 Results and Discussion

4.1 Validation. First of all, the grid independence study has been carried out to ensure that the selected case with appropriate grid number is accurate enough for the subsequent work. In the COMSOL MULTIPHYSICS, the computation time and memory requirements are strongly related to the number of DOF, which depends on the meshing type, the shape functions selected, and the number of dependent variables from the different physics. As shown in Fig. 3, four cases with different DOF numbers (36,510, 64,132, 92,838, and 139,560, respectively) have been investigated. It is

Table 4 Main parameters used by MOGA

Population size	100
Generation	60
Pareto fraction	0.6
Crossover fraction	0.8
Migration	0.2

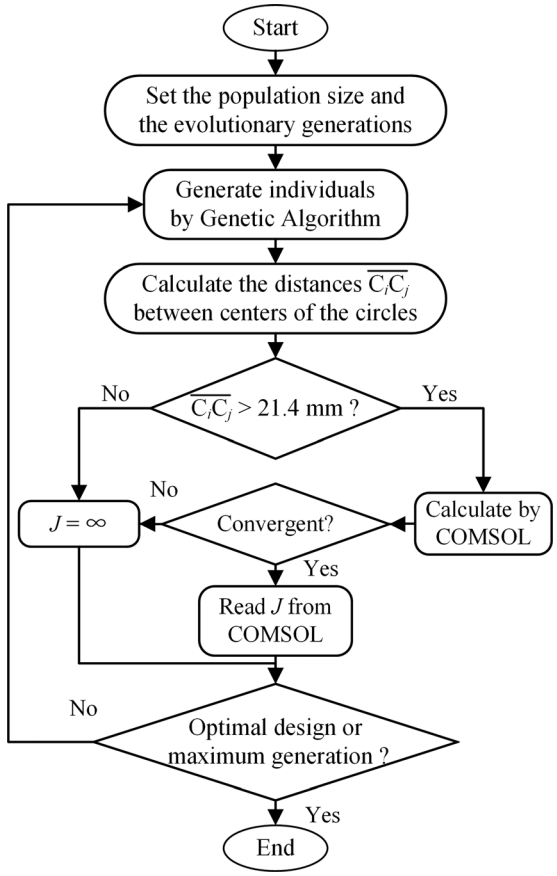

Fig. 2 Flowchart of the optimization procedure

confirmed that Δp varies approximately 1.5% and Nusselt number Nu varies approximately 1.2%, respectively, when DOF varies from 92,838 to 139,560. Therefore, the third meshing method is selected in this study in order to balance accuracy and computation time. The detailed grid systems for the selected calculation model are shown in Fig. 4, where the main region is based on the triangle grid with a maximum size of 4 mm^2 and the near-wall region is based on five layers of the quadrilateral grid, respectively. Besides, the near wall region is especially crucial for the k–ε model. In COMSOL MULTIPHYSICS, there assumes a small gap y_w between the computational domain and the physical wall, where y_w is automatically computed so that y plus ($y^+ = \rho u_\tau y_w/\mu$) is

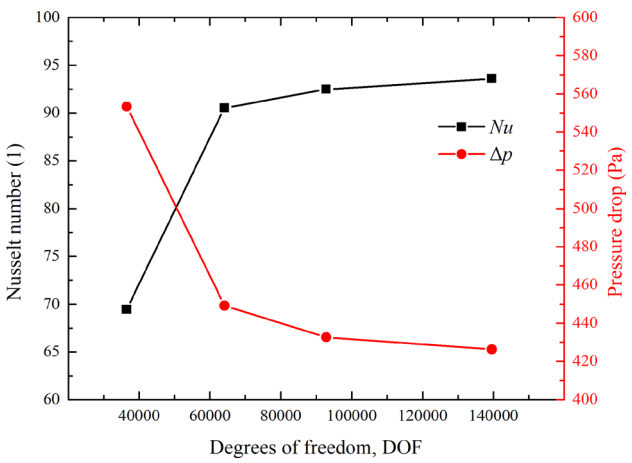

Fig. 3 The average Nu and Δp calculated by different DOF numbers with Re = 13,000 for the case 1

11.06. Subsequently, the corresponding wall function [35,36] is applied in this region. However, y_w would never be smaller than half the height of the boundary mesh cell in COMSOL MULTIPHYSICS. This means y^+ can be larger than 11.06 if the boundary mesh cell is too coarse, which further reduces the accuracy of the simulation. In this work, the average y^+ of the grid system is 11.062 and for the initial staggered case and 11.060 for the initial in-line case, respectively. Besides, the worst average y^+ for the optimization results is 11.301, which provide further evidence that the present grid system is accurate enough to apply the k–ε model.

Besides, both the Nusselt number Nu and the pressure drop Δp have been compared with the corresponding experimental correlations established by Žukauskas et al. [1]

$$\mathrm{Nu} = 0.35(S_T/S_L)^{0.2}\mathrm{Re}^{0.6}\mathrm{Pr}_f^{0.36}(\mathrm{Pr}_f/\mathrm{Pr}_w)^{0.25}\ (10^3 < \mathrm{Re} < 2\times 10^5) \tag{10}$$

$$\Delta p = \left(\frac{\xi}{\chi}\right)\chi\frac{1}{2}\rho\bar{u}^2 z \tag{11}$$

where S_T and S_L are the transverse and longitudinal tube pitches in the staggered arrangement, respectively. The Reynolds number, Re, is calculated according to the mean velocity in the minimum free cross section, $\bar{u}$. The factor (ξ/χ) and χ are given in diagrams by Žukauskas [1] according to the Re. Therefore, it can be obtained that Nu is 91.2 and Δp is 465 Pa by the experimental correlations when the Re is 13,000. Compared with the simulation results (Nu = 92.5 and Δp = 432.7 Pa), differences of the heat transfer and the pressure drop are 1.4% and 6.9%, respectively. These results show that the calculated values of performances agree well with the experimental values and computation cases can be applied in the optimization procedure.

4.2 Pareto Front. Figure 5 shows the Pareto fronts for two different initial cases after the multi-objective optimization. As it can be observed, the optimal q varies from 2708.27 W/m^2 to 3641.25 W/m^2 and the optimal Δp varies from 380.32 Pa to 1117.74 Pa for the case 1. On the other hand, for the case 2, the optimal q varies from 2047.56 W/m^2 to 3217.22 W/m^2 and the optimal Δp varies from 181.13 Pa to 674.21 Pa, respectively. Meanwhile, it is found that two Pareto fronts intersect around the point (−2795, 393), which indicates that there is a performance turning point for two different cases. The velocity comparison between two different cases around the turning point is illustrated in Fig. 6. When the $\Delta p < 393$ Pa, the optimal solutions by using the in-line model as the initial case will get better performances than those by using the staggered model as the initial case, while the opposite conclusion can be drawn when the $\Delta p > 393$ Pa.

Due to the difference between the initial arrangements, the maximum potential for case 1 or case 2 is also different. Figures 7 and 8 show the velocity fields and temperature fields for four optimal solutions selected from Pareto fronts (A–D shown in Fig. 5, which represents the solution with maximum q or minimum Δp for case 1 or case 2, respectively). It is obvious that the arrangement for solutions A and B is much more compact than that of C and D, which leads to a reduction of the free cross section. As a

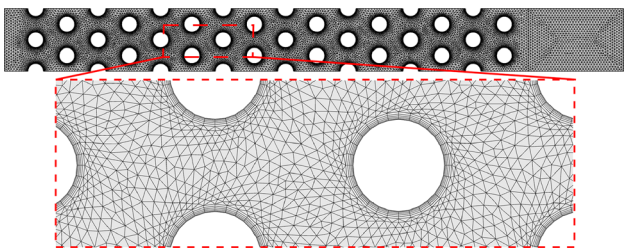

Fig. 4 Grid systems for calculation cases

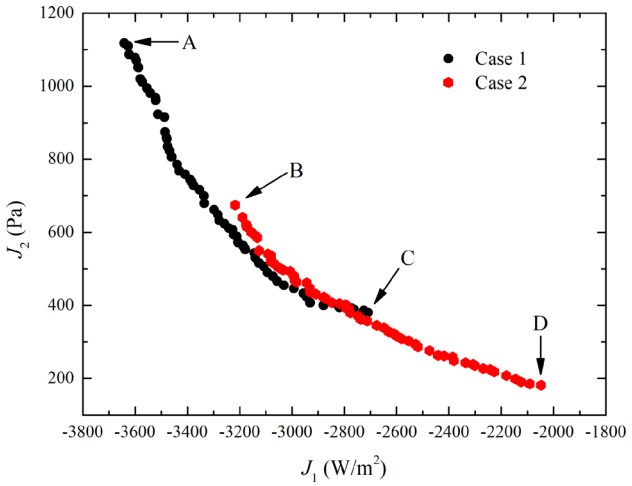

Fig. 5 Pareto fronts obtained by the multi-objective genetic algorithm

result, the flow velocity near the tube increases significantly and the flow dead zone is reduced obviously. However, it is too much cost that pays for heat transfer enhancement, which may be a great challenge for the pump. Hence, an appropriate solution from the Pareto front that improves the heat transfer performance without bringing too much pumping power is desired.

4.3 Technique for Order Preference by Similarity to an Ideal Solution Selection. As mentioned above, selecting the best solution from the alternatives based on the evaluation criteria is essential for industrial applications. In general, the subgoals of the multi-objective optimization problem are contradictory. The improvement of one objective on the Pareto front will cause the performance of others to be degraded, which means to simultaneously optimize all the objectives is not possible. However, different objective function could be compromised so that each of the subgoals is as optimal as possible by means of the multiple decision algorithms. After determining two ideal solutions, TOPSIS [33] is a practical and classical approach for ranking and selecting alternatives for the multi-objective optimization. The basic concept of TOPSIS is that the chosen alternative should have the longest distance from the negative ideal solution and the shortest distance from the positive ideal solution. In this work, the positive ideal solution has the minimum Δp and maximum q, while the negative ideal solution is just the opposite. The computational procedure of TOPSIS is as follows:

(1) Create a matrix $(x_{ij})_{m\times n}$ with m alternatives and n objectives.

(2) Normalize the matrix $(x_{ij})_{m\times n}$ to $(t_{ij})_{m\times n}$ by using the equation below:

$$t_{ij} = \frac{x_{ij}}{\sqrt{\sum_{i=1}^{m} x_{ij}^2}},\ i = 1, 2, \ldots, m,\ j = 1, 2, \ldots, n \tag{12}$$

(3) Obtain the weighted normalized matrix $(a_{ij})_{m\times n}$ by Eq. (9), where the weighted coefficient w_j is the default value (0.5, 0.5) to avoid involving the bias in this study

$$a_{ij} = w_j \times t_{ij},\ i = 1, 2, \ldots, m,\ j = 1, 2, \ldots, n \tag{13}$$

(4) Determine the positive ideal alternative a^+ and the negative ideal alternative a^-

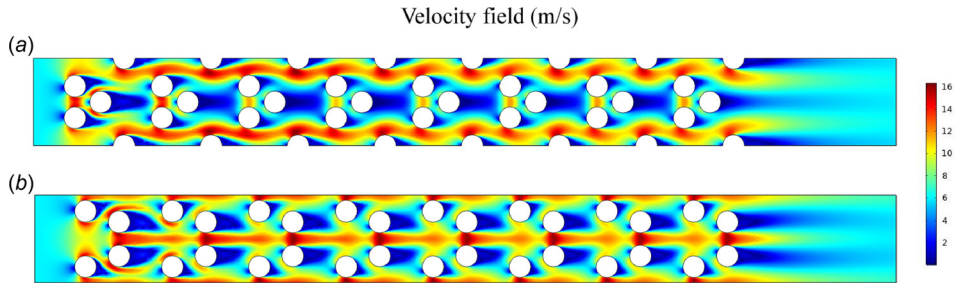

Fig. 6 Velocity comparison between two different cases around the turning point. (*a*) Case 1, (J_1, J_2) = (−2804.4, 393.68) and (*b*) case 2, (J_1, J_2) = (−2791.5, 393.10).

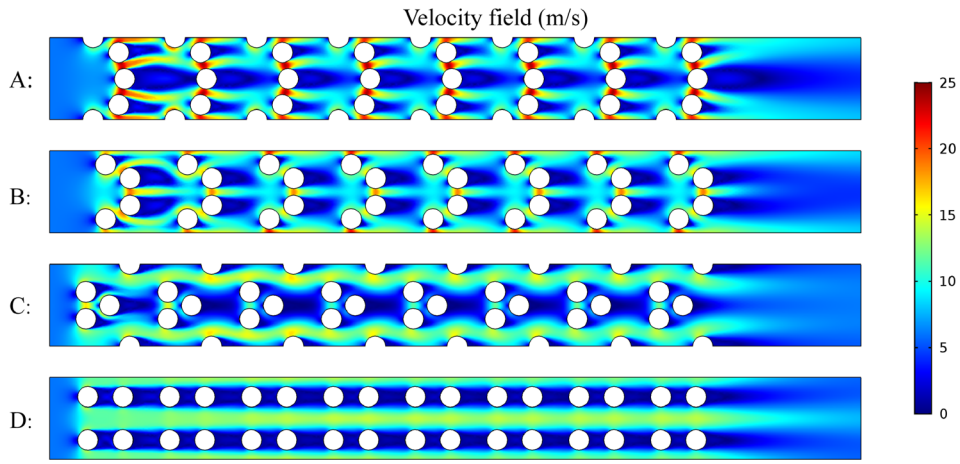

Fig. 7 Velocity fields of four optimal solutions selected from the Pareto front

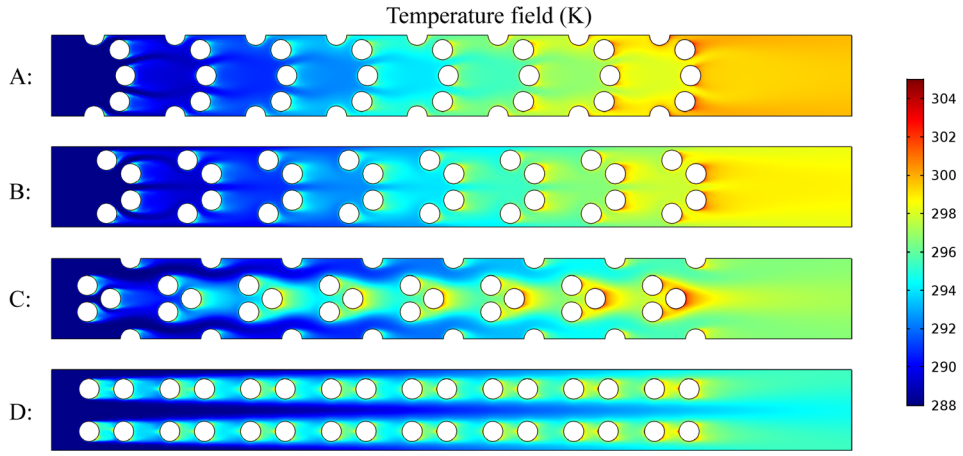

Fig. 8 Temperature fields of four optimal solutions selected from the Pareto front

$$a^{+} = (\min[a_{11}, \ldots a_{m1}], \min[a_{12}, \ldots a_{m2}], \ldots, \min[a_{1n}, \ldots a_{mn}]) \tag{14}$$

$$a^{-} = (\max[a_{11}, \ldots a_{m1}], \max[a_{12}, \ldots a_{m2}], \ldots, \max[a_{1n}, \ldots a_{mn}]) \tag{15}$$

(5) Calculate the distance between the target alternative a_i and the positive ideal alternative a^{+}, and the distance between the target alternative a_i and the negative ideal alternative a^{-}

$$d_i^{+} = \sqrt{\sum_{j=1}^{n} (a_{ij} - a_j^{+})^2},\ i = 1, 2, \ldots, m, j = 1, 2, \ldots, n \tag{16}$$

$$d_i^{-} = \sqrt{\sum_{j=1}^{n} (a_{ij} - a_j^{-})^2},\ i = 1, 2, \ldots, m, j = 1, 2, \ldots, n \tag{17}$$

(6) Calculate the relative closeness to the ideal solution of alternatives

$$c_i = \frac{d_i^{-}}{d_i^{+} + d_i^{-}},\ i = 1, 2, \ldots, m \tag{18}$$

(7) Rank the alternatives according to the values of c_i, and the final compromise solution a_{final} is

$$a_{\text{final}} = a \in \max(c_i) \tag{19}$$

Figure 9 shows the detailed ranking results according to the above equations and Table 5 gives the best solution with optimal coordinates and performances determined by TOPSIS. All the individuals from both case 1 and case 2 have participated in the selection procedure. Even all the solutions are noninferior solutions; it can be found that the ranking score, which represents the overall performance, shows an obvious difference along the Pareto front. The best solution is selected from the case 2 with ranking score $c = 0.7737$, while the worst one is from the case 1 with $c = 0.2515$, respectively. Besides, individuals at the endpoints of the Pareto front have lower ranking scores, which means simply improving a certain performance will lead to a decline in overall performance.

4.4 Performances Comparison. Comparisons of the velocity field and the temperature field between the best solution determined by TOPSIS and the initial in-line arrangement are plotted in Figs. 10 and 11, respectively. Compared with the initial tube

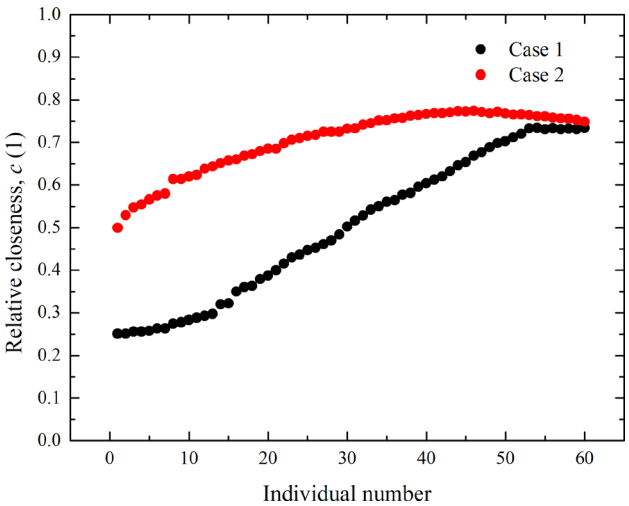

Fig. 9 Ranking results of two Pareto fronts

bundle, even-numbered rows of tubes are closer behind previous odd-numbered rows of tubes and deviate slightly. As a result, there is more air flow between two tubes and the thickness of the thermal boundary layer near the rear area of odd-numbered rows is reduced. The flow behavior could be observed clearly by the velocity vectors shown in Fig. 12. It is found that the flow pattern has changed at the rear area of odd-numbered rows since the previous recirculation zone is disappeared in this region. Furthermore, the velocity at the front area of odd-numbered rows is increased by the previous bundle unit, which will also enhance the local heat transfer performance. To sum up the above content, we could draw a brief conclusion that the optimized flow field structure can reduce the flow dead zone and recirculation zone, which will improve the performance of the heat transfer.

To demonstrate the heat transfer enhancement in detail, the performance comparison between the optimal solution selected by TOPSIS and the initial one is illustrated in Fig. 13, which includes both the front half and the rear half of each tube. Since more air flow exists between two tubes for the tube bundle unit, the rear half of odd-numbered rows and the front half of even-numbered

Table 5 The best solution determined by TOPSIS

a_1	a_2	a_3	a_4	Δp (Pa)	q (W/m^2)	Score
39.98	14.49	61.06	18.51	263.66	2441.91	0.7737

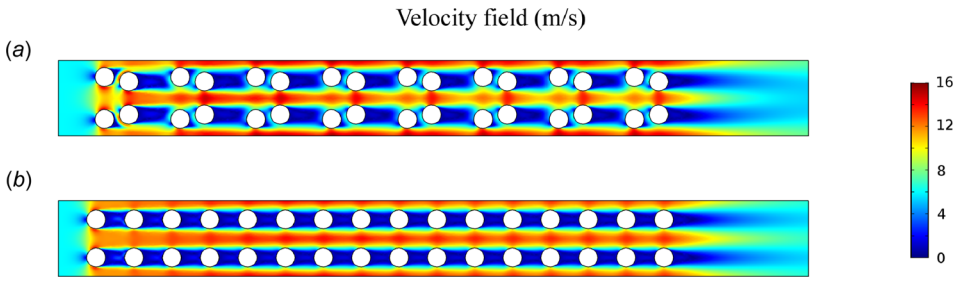

Fig. 10 Comparison of the velocity field. (*a*) The best solution determined by TOPSIS. (*b*) The initial in-line arrangement.

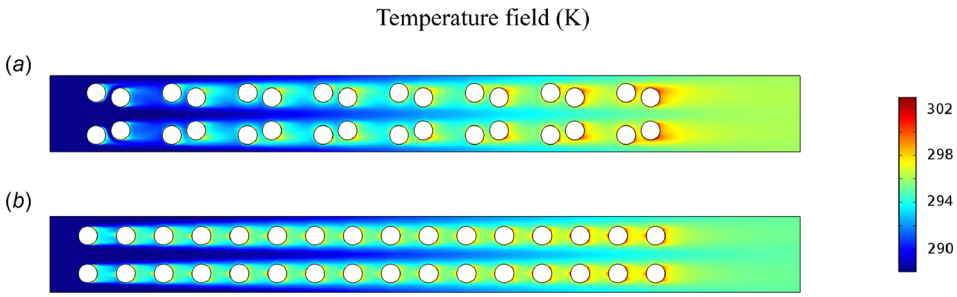

Fig. 11 Comparison of the temperature field. (*a*) The best solution determined by TOPSIS. (*b*) The initial in-line arrangement.

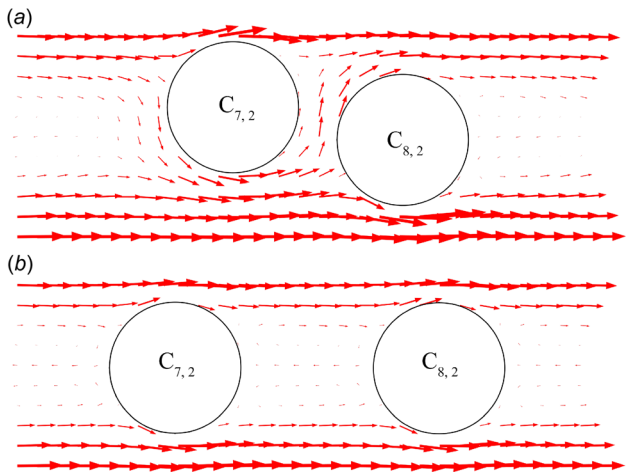

Fig. 12 Velocity vectors around the tubes $C_{7,2}$ and $C_{8,2}$. (*a*) The best solution determined by TOPSIS. (*b*) The initial in-line arrangement.

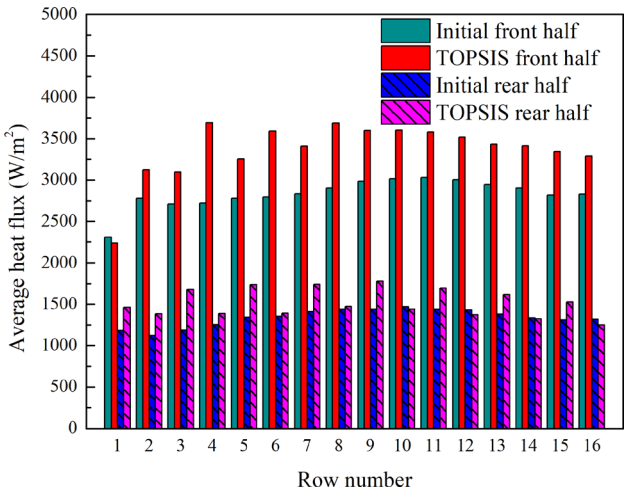

Fig. 13 Average heat flux of front half, rear half for each row of tubes

rows improve significantly. For the entire tube bundle, the average heat flux for these two parts increases by 23.86% and 21.73%, respectively. Meanwhile, the previous tube bundle unit also has an influence on the next tube bundle, which results in a 15.82% increase in the average heat flux for the front half of odd-numbered rows. However, the heat transfer performance increases limitedly (about 2.83%) for the rear half of even-numbered rows since the flow state has substantially no change in this area. The above results provide further evidence that the initial arrangement of the tube bundle is not appropriate, and the relative position of tubes has a significant influence on the heat transfer.

Next, the optimal solutions under different evaluation criteria are investigated, where solutions A–D are selected from the Pareto front as mention previously. All the results including both the q and the Δp are plotted in Fig. 14. Compared with the arrangement with maximum q, the optimal solution determined by TOPSIS decreases about 32.94% in the q but decreases about 76.41% in the Δp. Hence, even though the heat transfer performance has a degradation, the power consumption is reduced more significantly. On the other hand, compared with the one selected by TOPSIS, solution D has a further reduction in Δp (from 76.41% to 87.80%), but the heat transfer performance also further decreases from 32.94% to 43.77%. It is obvious that this cost reduction is unworthy since too much performance is sacrificed. The above results indicate that TOPSIS is an effective method to determine the best compromise from the Pareto front.

5 Conclusion

This paper offers a new strategy to design the arrangement of a tube bundle by combining CFD method and Pareto-based multi-objective optimization technique. The minimum pressure drop Δp and the maximum average heat flux of tubes q are two conflicting objectives simultaneously considered. The performances of the proposed tube bundle are decided by four coordinate variables

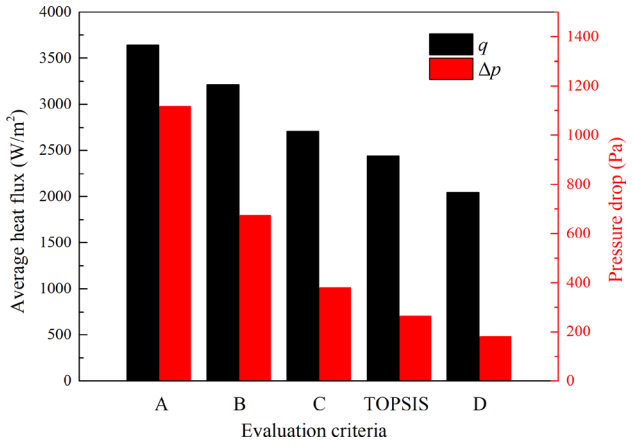

Fig. 14 Performances of optimal tube bundles under different evaluation criteria

and all the simulation models are calculated by the finite element software. Then, the MOGA is used to find the Pareto solutions of the multi-objective problem. After combining optimal solutions from two symmetric cases used to reducing computing time, TOPSIS method is applied to determine the best compromise solution from the Pareto front. The main conclusions can be drawn as follows:

(1) The performances of optimal tube bundle in comparison with those of initial one show that the arrangement of tubes indeed has a significant influence on heat transfer and flow resistance. For the case 1, the optimal q varies from 2708.27 W/m^2 to 3641.25 W/m^2 and the optimal Δp varies from 380.32 Pa to 1117.74 Pa, respectively. For the case 2, the optimal q varies from 2047.56 W/m^2 to 3217.22 W/m^2 and the optimal Δp varies from 181.13 Pa to 674.21 Pa, respectively.

(2) The optimized flow-field structure reduces the flow dead zone and recirculation zone, which further improves the performance of the heat transfer. As a result, the heat transfer performance has increased by about 17.05% after the optimization.

(3) The comparison between the optimal solution selected by TOPSIS and solutions with maximum q or minimum Δp indicates that TOPSIS method can reduce the Δp of the tube bundle without sacrificing too much heat transfer performance.

These above results show that this multi-objective optimization for the tube bundle, where the CFD software, the MOGA, and the TOPSIS are simultaneously applied to find the best compromise solution is a comprehensive method for the further practical application, even though 6000 simulation scenarios need to be solved.

Funding Data

- National Natural Science Foundation of China (Grant Nos. 51776079 and 51736004; Funder ID: 10.13039/501100001809).
- National Key Research and Development Program of China (Grant No. 2017YFB0603501-3; Funder ID: 10.13039/501100002855).

Nomenclature

a = design variable to optimize
c = relative closeness to the ideal solution
c_p = specific heat
D = tube diameter
J = objective function
L = length
Nu = Nusselt number
p = pressure
Δp = pressure drop
q = average heat flux
Re = Reynolds number
S_L = longitudinal tube-pitch
S_T = transverse tube-pitch
T = temperature
u = flow velocity
W = width
x, y, z = orthogonal coordinate system

Greek Symbols

λ = thermal conductivity
μ = dynamic viscosity
ρ = fluid density

Superscript

f = fluid
in = inlet
out = outlet
s = solid
unit = design unit
w = wall

References

[1] Žukauskas, A., 1972, "Heat Transfer From Tubes in Crossflow," Adv. Heat Transfer, **8**, pp. 93–160.
[2] Matos, R. S., Vargas, J. V. C., Laursen, T. A., and Saboya, F. E. M., 2001, "Optimization Study and Heat Transfer Comparison of Staggered Circular and Elliptic Tubes in Forced Convection," Int. J. Heat Mass Transfer, **44**(20), pp. 3953–3961.
[3] Khan, W. A., Culham, J. R., and Yovanovich, M. M., 2006, "Convection Heat Transfer From Tube Banks in Crossflow: Analytical Approach," Int. J. Heat Mass Transfer, **49**(25–26), pp. 4831–4838.
[4] Liu, W., Liu, P., Wang, J. B., Zheng, N. B., and Liu, Z. C., 2018, "Exergy Destruction Minimization: A Principle to Convective Heat Transfer Enhancement," Int. J. Heat Mass Transfer, **122**, pp. 11–21.
[5] Liu, W., Liu, P., Dong, Z. M., Yang, K., and Liu, Z. C., 2019, "A Study on the Multi-Field Synergy Principle of Convective Heat and Mass Transfer Enhancement," Int. J. Heat Mass Transfer, **134**, pp. 722–734.
[6] Wang, X. T., Zheng, N. B., Liu, P., Liu, Z. C., and Liu, W., 2017, "Numerical Investigation of Shell Side Performance of a Double Shell Side Rod Baffle Heat Exchanger," Int. J. Heat Mass Transfer, **108**, pp. 2029–2039.
[7] Wang, X. T., Liang, Y. M., Sun, Y., Liu, Z. C., and Liu, W., 2019, "Experimental and Numerical Investigation on Shell-Side Performance of a Double Shell-Pass Rod Baffle Heat Exchanger," Int. J. Heat Mass Transfer, **132**, pp. 631–642.
[8] Qian, Z., Li, Y., and Rao, Z. H., 2016, "Thermal Performance of Lithium-Ion Battery Thermal Management System by Using Mini-Channel Cooling," Energy Convers. Manage., **126**, pp. 622–631.
[9] Lin, L., Zhao, J., Lu, G., Wang, X. D., and Yan, W. M., 2017, "Heat Transfer Enhancement in Microchannel Heat Sink by Wavy Channel With Changing Wavelength/Amplitude," Int. J. Therm. Sci., **118**, pp. 423–434.
[10] Li, P. X., Liu, Z. C., Liu, W., and Chen, G., 2015, "Numerical Study on Heat Transfer Enhancement Characteristics of Tube Inserted With Centrally Hollow Narrow Twisted Tapes," Int. J. Heat Mass Transfer, **88**, pp. 481–491.
[11] Kumar Rout, P., and Kumar Saha, S., 2013, "Laminar Flow Heat Transfer and Pressure Drop in a Circular Tube Having Wire-Coil and Helical Screw-Tape Inserts," ASME J. Heat Transfer, **135**(2), p. 021901.
[12] Yang, L. B., Han, H. Z., Li, Y. J., and Li, X. M., 2015, "A Numerical Study of the Flow and Heat Transfer Characteristics of Outward Convex Corrugated Tubes With Twisted-Tape Insert," ASME J. Heat Transfer, **138**(2), p. 024501.
[13] Webb, R. L., 1981, "Performance Evaluation Criteria for Use of Enhanced Heat Transfer Surfaces in Heat Exchanger Design," Int. J. Heat Mass Transfer, **24**(4), pp. 715–726.
[14] Yun, J. Y., and Lee, K. S., 2000, "Influence of Design Parameters on the Heat Transfer and Flow Friction Characteristics of the Heat Exchanger With Slit Fins," Int. J. Heat Mass Transfer, **43**(14), pp. 2529–2539.
[15] Liu, W., Liu, Z. C., and Ma, L., 2012, "Application of a Multi-Field Synergy Principle in the Performance Evaluation of Convective Heat Transfer Enhancement in a Tube," Chin. Sci. Bull., **57**(13), pp. 1600–1607.
[16] Deb, K., Pratap, A., Agarwal, S., and Meyarivan, T., 2002, "A Fast and Elitist Multiobjective Genetic Algorithm: NSGA-II," IEEE Trans. Evol. Comput., **6**(2), pp. 182–197.
[17] Long, R., Li, B. D., Liu, Z. C., and Liu, W., 2018, "Reverse Electrodialysis: Modelling and Performance Analysis Based on Multi-Objective Optimization," Energy, **151**, pp. 1–10.

[18] Ge, Y., Liu, Z. C., Sun, H. N., and Liu, W., 2018, "Optimal Design of a Segmented Thermoelectric Generator Based on Three-Dimensional Numerical Simulation and Multi-Objective Genetic Algorithm," Energy, **147**, pp. 1060–1069.
[19] Ge, Y., Liu, Z. C., and Liu, W., 2016, "Multi-Objective Genetic Optimization of the Heat Transfer for Tube Inserted With Porous Media," Int. J. Heat Mass Transfer, **101**, pp. 981–987.
[20] Sun, H. N., Ge, Y., Liu, W., and Liu, Z. C., 2019, "Geometric Optimization of Two-Stage Thermoelectric Generator Using Genetic Algorithms and Thermodynamic Analysis," Energy, **171**, pp. 37–48.
[21] Salviano, L. O., Dezan, D. J., and Yanagihara, J. I., 2015, "Optimization of Winglet-Type Vortex Generator Positions and Angles in Plate-Fin Compact Heat Exchanger: Response Surface Methodology and Direct Optimization," Int. J. Heat Mass Transfer, **82**, pp. 373–387.
[22] Vignesh Ram, P. S., Setoguchi, T., and Kim, H. D., 2016, "Effects of Vortex Generator on Cylindrical Protrusion Aerodynamics," J. Therm. Sci., **25**(1), pp. 7–12.
[23] Xie, G. N., Sunden, B., Wang, Q. W., and Tang, L. H., 2009, "Performance Predictions of Laminar and Turbulent Heat Transfer and Fluid Flow of Heat Exchangers Having Large Tube-Diameter and Large Tube-Row by Artificial Neural Networks," Int. J. Heat Mass Transfer, **52**(11–12), pp. 2484–2497.
[24] Wang, X. T., Zheng, N. B., Liu, Z. C., and Liu, W., 2018, "Numerical Analysis and Optimization Study on Shell-Side Performances of a Shell and Tube Heat Exchanger With Staggered Baffles," Int. J. Heat Mass Transfer, **124**, pp. 247–259.
[25] Varol, Y., Oztop, H. F., and Avci, E., 2008, "Estimation of Thermal and Flow Fields Due to Natural Convection Using Support Vector Machines (SVM) in a Porous Cavity With Discrete Heat Sources," Int. Commun. Heat Mass Transfer, **35**(8), pp. 928–936.
[26] Hao, X. J., An, X. R., Wu, B., and He, S. P., 2018, "Application of a Support Vector Machine Algorithm to the Safety Precaution Technique of Medium-Low Pressure Gas Regulators," J. Therm. Sci., **27**(1), pp. 74–77.
[27] Cheng, C. H., Chan, C. K., and Lai, G. J., 2008, "Shape Design of Millimeter-Scale Air Channels for Enhancing Heat Transfer and Reducing Pressure Drop," Int. J. Heat Mass Transfer, **51**(9–10), pp. 2335–2345.
[28] Cheng, C. H., and Chang, M. H., 2003, "A Simplified Conjugate-Gradient Method for Shape Identification Based on Thermal Data," Numer. Heat Transfer, Part B, **43**(5), pp. 489–507.
[29] Liu, Z. C., Zhu, S. P., Ge, Y., Shan, F., Zeng, L. P., and Liu, W., 2017, "Geometry Optimization of Two-Stage Thermoelectric Generators Using Simplified Conjugate-Gradient Method," Appl. Energy, **190**, pp. 540–552.
[30] Daróczy, L., Janiga, G., and Thévenin, D., 2014, "Systematic Analysis of the Heat Exchanger Arrangement Problem Using Multi-Objective Genetic Optimization," Energy, **65**, pp. 364–373.
[31] Ge, Y., Shan, F., Liu, Z. C., and Liu, W., 2017, "Optimal Structural Design of a Heat Sink With Laminar Single Phase Flow Using CFD Based Multi-Objective Genetic Algorithm," ASME J. Heat Transfer, **140**(2), p. 022803.
[32] Ge, Y., Wang, S. C., Liu, Z. C., and Liu, W., 2019, "Optimal Shape Design of a Minichannel Heat Sink Applying Multi-Objective Optimization Algorithm and Three-Dimensional Numerical Method," Appl. Therm. Eng., **148**, pp. 120–128.
[33] Hwang, C. L., Lai, Y. J., and Liu, T. Y., 1993, "A New Approach for Multiple Objective Decision Making," Comput. Oper. Res., **20**(8), pp. 889–899.
[34] Wilcox, D. C., 1998, *Turbulence Modeling for CFD*, DCW Industries, La Canada, CA.
[35] Grotjans, H., and Menter, F., 1998, "Wall Functions for General Application {CFD} Codes," Fourth European Computational Fluid Dynamics Conference, Athens, Greece, Sept. 7–11, pp. 1112–1117.
[36] Kuzmin, D., Mierka, O., and Turek, S., 2007, "On the Implementation of the κ-ε Turbulence Model in Incompressible Flow Solvers Based on a Finite Element Discretisation," Int. J. Comput. Sci. Math., **1**(2/3/4), p. 193.